ACS Chemical Neuroscience

pubs.acs.org/chemneuro Research Article

Repurposing Antimicrobial Protegrin-1 as a Dual-Function Amyloid Inhibitor *via* Cross-seeding

Yijing Tang, Dong Zhang, and Jie Zheng*

Cite This: *ACS Chem. Neurosci.* 2023, 14, 3143−3155 Read Online

ACCESS | Metrics & More | Article Recommendations | Supporting Information

ABSTRACT: Amyloids and antimicrobial peptides have traditionally been recognized as distinct families with separate biological functions and targets. However, certain amyloids and antimicrobial peptides share structural and functional characteristics that contribute to the development of neurodegenerative diseases. Specifically, the aggregation of amyloid-β (Aβ) and microbial infections are interconnected pathological factors in Alzheimer's disease (AD). In this study, we propose and demonstrate a novel repurposing strategy for an antimicrobial peptide of protegrin-1 (PG-1), which exhibits the ability to simultaneously prevent Aβ aggregation and microbial infection both in vitro and in vivo. Through a comprehensive analysis using protein, cell, and worm assays, we uncover multiple functions of PG-1 against Aβ, including the following: (i) complete inhibition of Aβ aggregation at a low molar ratio of PG-1/Aβ = 0.25:1, (ii) disassembly of the preformed Aβ fibrils into amorphous aggregates, (iii) reduction of Aβ-induced cytotoxicity in SH-SY5Y cells and transgenic GMC101 nematodes, and (iv) preservation of original antimicrobial activity against P.A., *E.coli.*, S.A., and S.E. strains in the presence of Aβ. Mechanistically, the dual anti-amyloid and anti-bacterial functions of PG-1 primarily arise from its strong binding to distinct Aβ seeds (K_D = 1.24−1.90 μM) through conformationally similar β-sheet associations. This work introduces a promising strategy to repurpose antimicrobial peptides as amyloid inhibitors, effectively targeting multiple pathological pathways in AD.

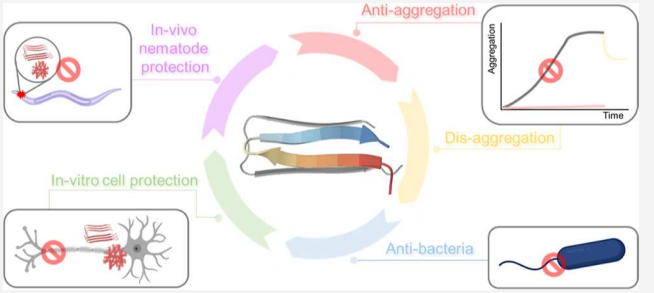

KEYWORDS: *protegrin-1, cross-seeding, microbial infection, Alzheimer's disease, amyloid aggregation, amyloid inhibition*

1. INTRODUCTION

With the increase in life expectancy and aging population, Alzheimer's disease (AD), the most common, multifactorial, age-related neurodegenerative disorder, will become ever more prevalent in society.[1−3] AD leads to severe cognitive impairment, memory decline, and loss of executive functions and consciousness due to the functional loss of the synapses and neurons in the cortex and hippocampus of the midbrain. While there is currently no cure for AD and available treatments are only aimed at relieving the symptoms or delaying the progression of the symptoms, decades of the basic, translational, and clinical research efforts have revealed distinct mechanisms[3] (*e.g.*, amyloid aggregation, transmitter imbalance, and neuroinflammation) and risk factors (*e.g.*, age, genetics, heart disease, and diabetes.) and described the different molecular and cellular pathways involved in AD pathogenesis. The continued failure of drugs in the clinical treatment of AD could be mainly due to two aspects: (i) it may be too late to target Aβ-related pathologies to prevent the progression of AD symptoms and (ii) the non-aggregation role of Aβ in the pathogenesis of AD still remains poorly understood.

As a multifactorial and chronic disease, protein misfolding/aggregation and neuroinflammation are widely recognized as two key pathological mechanisms leading to AD dementia. The protein misfolding/aggregation mechanism is built on massive evidence from *in vitro*, *in vivo*, and *in silico* studies accounting for 60−80% of AD cases.[2] The most prominent pathological hallmarks of AD are the formation of extracellular senile plaques composed of β-amyloid (Aβ) fibrils and intracellular neurofibrillary tangles by tau protein aggregates.[4,5] While the exact mechanism by which Aβ aggregation induces neuronal death is not yet known, it is generally acknowledged that Aβ aggregates rich in β-sheets, especially oligomeric intermediates, are highly toxic and induce cell death by disrupting the integrity of cell membranes and the functions of membrane-incorporated proteins. This protein misfolding/aggregation mechanism is also generally applicable to other neurodegenerative diseases, including Parkinson's disease by α-synuclein aggregation and type II diabetes by hIAPP aggregation. In parallel, neuroinflammation, characterized by elevated blood levels of circulating proinflammatory cytokines,

Received: May 3, 2023
Accepted: August 3, 2023
Published: August 17, 2023

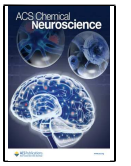

has also been implicated as another key factor in promoting neurodegeneration in AD.[6] Proinflammatory cytokines (*e.g.*, IL-1β, TNFα, and IL-6) not only promote the overproduction of Aβ of various lengths (*e.g.*, Aβ_{40} and Aβ_{42}) by increasing the cleavage of APP by β- and γ-secretases but also inhibit the ability of microglia to phagocytose Aβ. In turn, the increased levels of Aβ trigger the microglial production and spreading of cytokines (IL-1β, TNFα, and IL-6). This vicious cycle continuously increases the levels of Aβ and inflammatory proteins in the blood while reducing the clearance of Aβ, all of which lead to the promotion of Aβ aggregation and Aβ-induced neuroinflammation in the brain.

In addition to Aβ-triggered neuroinflammation, a number of specific bacterial and viral infections can also induce AD-associated neuroinflammation, including infections by oncogenic viruses[7,8] (*e.g.*, EBV, HBV, and HHV-6 DNA sequences), bacteria[9,10] (*e.g.*, *Borrelia burgdorferi* and *Treponema* species), fungi[11] (*e.g.*, *Cryptococcus curvatus* and *Botrytis cinerea*), and herpetic viruses[12] (*e.g.*, HSV-1 and CMV). These bacteria, viruses, and fungi were found in high concentrations at very close proximity to amyloid plaques in AD postmortem brains. The presence of these pathogens in high concentrations induces the chronic overproduction of inflammatory cytokines[13] and antibodies/antigens,[14,15] which triggers the neuroinflammation and neurodegeneration by physical disruption of neuronal process and activity in AD.[16−18] More importantly, recent studies have shown bi-directional communication between microbial pathogens and Aβ aggregates,[8] which triggers multiple pathophysiological effects such as synaptic dysfunctioning, neuronal excitotoxicity, oxidative stress, mitochondrial alterations, and disturbed calcium homeostasis, although mechanistic understanding of this communication between the pathogens and Aβ still remains elusive. Specifically, FapC amyloid fragments (FapCS) of *Pseudomonas aeruginosa* are shown to cross-interact with Aβ to promote Aβ aggregation, and this cross-seeding-induced Aβ promotion further impairs the cognitive function of zebrafish.[19] In a similar fashion, extracellular DNA in bacteria may directly or indirectly interact with Aβ and other amyloid proteins to promote amyloid oligomerization and produce toxic effects on cells.[20] On the other hand, amyloid proteins including Aβ could act as active metabolites of the innate immune system to influence microbial behaviors. Aβ oligomers can bind to the carbohydrates of microbial cell walls through the heparin-binding domain, thereby reducing the microbial adhesion to host cells and the agglutination and entrapment of microbes in cells, nematodes, and AD-infection mouse models.[21]

Based on these findings, simultaneous targeting of Aβ misfolding and Aβ-induced neuroinflammation may provide a promising "kill two birds with one stone" strategy to interrupt Aβ-triggered AD pathology. Conceptually, the discovery or repurposing of antibacterial peptides, with intrinsic antimicrobial activity, as amyloid inhibitors is a plausible strategy to achieve anti-neuroinflammation and anti-amyloid functions simultaneously. Although AMPs and amyloid peptides are considered at first glance to be two distinct peptide families with distinct biological targets and functions,[22] recent studies have found that both amyloid and antimicrobial peptides are similar to each other in certain structural and functional features. First, AMPs including protegrin-1 (PG-1),[23] plantaricin A,[24] uperin 3.5,[22] magainin,[25,26] and dermaseptin S9[27] have been shown to possess the ability to form β-sheet-rich amyloid fibrils, which were morphologically similar to the classic amyloid fibrils. In parallel, several amyloid peptides including Aβ, hIAPP, α-syn, and SAA[28−32] have shown certain antibacterial activity against *Candia albicans*, *Escherichia coli*, and *Staphylococcus epidermidis*[33−36] and antiviral activity against influenza virus A, herpes simplex virus (HSV), H3N2, and H1N1.[37,38] Especially, Aβ had an antimicrobial potency equivalent to or greater than that of LL37, suggesting that Aβ might belong to a family of AMPs contributing to proinflammatory activities in AD. Second, several studies have found that both amyloid and antimicrobial peptides have similar killing mechanisms to kill the host target cells and pathogens by forming nonspecific ion channels in the cell membranes. Third, structural studies further showed that some amyloid and antimicrobial peptides can form β-sheet-rich structures, which exhibit a strong binding affinity to cell membranes for catalyzing toxin-like channel formation and membrane depolarization.

Given that amyloid and antimicrobial peptides are mutually similar in certain structural and functional features,[39,40] here, we discovered a new biological function of PG-1, an antimicrobial innate immune peptide that wards off invading pathogens, as an amyloid inhibitor against Aβ aggregation/cytotoxicity and microbial infection, both of which are involved in different pathological pathways toward the onset and progression of AD. A main reason for choosing PG-1 is that it can fold into a β-hairpin conformation in bulk solution,[41,42] on POPC and POPC/POPG lipid bilayers,[43] and even inside the cell membrane.[44] The similar β-sheet structure increases the possibility of Aβ and PG-1 interactions (*i.e.*, cross-seeding) *via* β-sheet-to-β-sheet association.[45,46] Collective results showed that PG-1 was capable of cross-seeding with Aβ at sub-stoichiometric molar ratios (*i.e.*, $\leq$equimolar) to execute its multiple functions, including (i) complete inhibition of Aβ aggregation at a very small dose of PG-1 (5 μM at a molar ratio of PG-1/Aβ = 0.25:1); (ii) breakdown of preformed Aβ fibrils into small pieces; (iii) Aβ-induced toxicity reduction in SH-SY5Y neuron cells and transgenic *C. elegans*; and (iv) retention of high antibacterial activity against four bacterial strains of both Gram-negative and Gram-positive types. The repurposing of PG-1 with novel Aβ-inhibitory functions mainly stems from its ability to interact with various Aβ species in different aggregation states, in which PG-1 was able to (i) stabilize the native folded structure of Aβ monomers to prevent their further misfolding and aggregation; (ii) reduce the aggregation kinetics by remodeling Aβ aggregation pathways; and (iii) act as "β-sheet breakers" to break down the preformed Aβ fibrils. Building upon the concept of cross-seeding, our study has identified PG-1 as a highly promising dual-functional amyloid inhibitor with the ability to effectively hinder both amyloid formation and bacterial growth. This finding not only paves the way for the development of multifunctional drugs targeting various factors involved in amyloid diseases but also presents a compelling alternative to conventional single-target therapeutics.

2. RESULTS AND DISCUSSION

2.1. Cross-seeding of PG-1 with Monomeric Aβ Inhibits Amyloid Aggregation. Considering that both PG-1 and Aβ are able to self-assemble into similar β-sheet-rich aggregates, we propose a "like-interacts-like" mechanism, *i.e.*, PG-1 is predicted to interact strongly with Aβ through conformationally similar β-structure association, in which the enhanced interactions between PG-1 and Aβ will in turn

https://doi.org/10.1021/acschemneuro.3c00293
ACS Chem. Neurosci. 2023, 14, 3143−3155

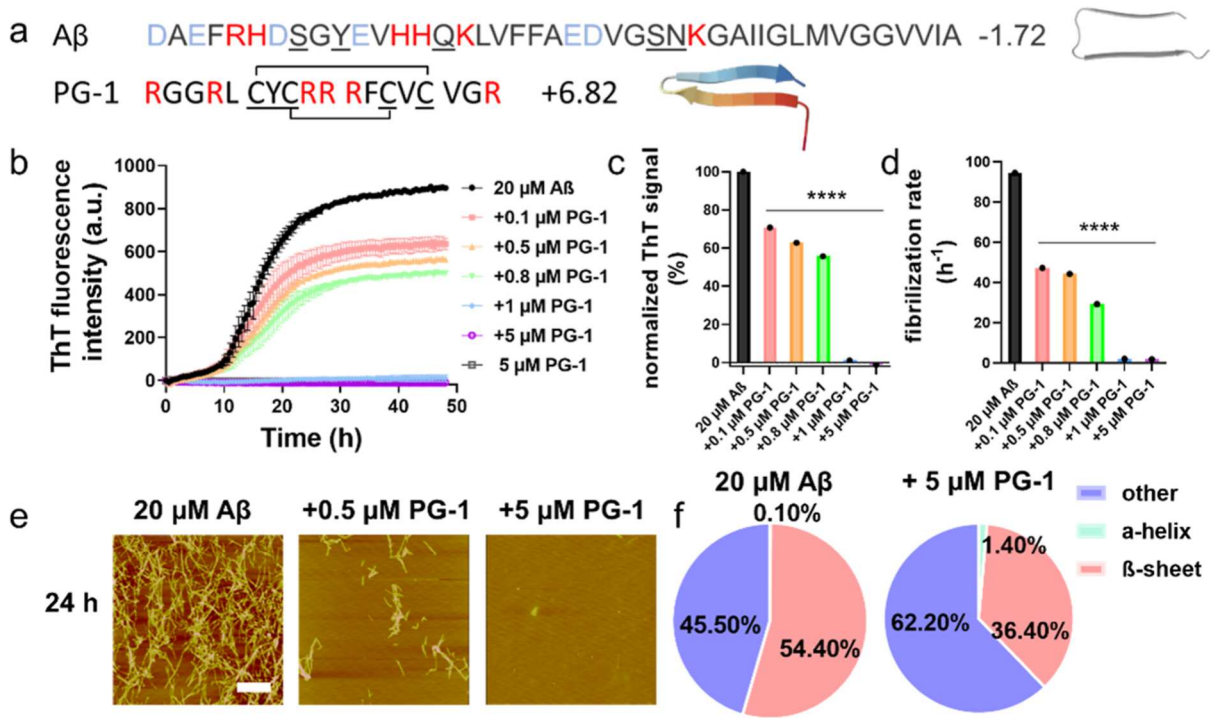

Figure 1. Cross-seeding of PG-1 with Aβ to inhibit Aβ aggregation. (a) Sequence and structure of Aβ and PG-1 with a folded β-rich-structure. Color ID: polar residues (underline), non-polar residues (black), negatively charged residues (blue), and positively charged residues (red). (b) Dose-dependent inhibition effect of PG-1 (0.1−5 μM) on Aβ (20 μM) aggregation by ThT fluorescence assays. All data represent mean ± standard error of triplicate measurements. (n = 3). Aggregation kinetics analysis of Aβ in the presence and absence of PG-1 in terms of (c) final normalized ThT intensity and (d) fibrillization rate. Final ThT fluorescence of pure Aβ aggregation is set to 100% and used as a basis for defining the relative ThT fluorescence ratio of PG-1-Aβ cross-seeding. A t-test was conducted to analyze the data comparing Aβ treated with PG-1 to pure Aβ (n = 3). (*p < 0.05, **p < 0.01, ***p < 0.005, and ****p < 0.001). (e) AFM images of pure Aβ sample (20 μM) and cross-seeding Aβ-PG-1 samples (20 μM/0.1−5 μM) after 24 h incubation. Scale bars are 1 μm. (f) Secondary structure distributions of pure Aβ sample (20 μM) and cross-seeding Aβ-PG-1 samples (20 μM/5 μM) after 48 h incubation.

competitively reduce Aβ−Aβ self-interaction, thereby inhibiting Aβ aggregation (Figure 1a). To test this hypothesis, we first investigated the potential inhibition effect of PG-1 on Aβ aggregation by co-incubating freshly prepared Aβ with PG-1 at different molar ratios in the range of 0.005−0.25 at 37 °C for 48 h. As shown in Figure 1b, pure PG-1 (5 μM) did not produce any fluorescence signal, indicating (i) the non-amylogenic nature of PG-1 at 5 μM and (ii) the absence of any ThT signal from PG-1 self-aggregation contributing to PG-1-Aβ cross-seeding. As another control, pure Aβ (20 μM) alone produced a typical nucleation−polymerization aggregation profile, starting with a lag phase of ∼9 h, followed by a rapid growth phase of 9−25 h, and ending at a stable ThT plateau of ∼895 a.u. When co-incubating non-amylogenic PG-1 (0−5 μM) with Aβ (20 μM), PG-1 at all tested sub-stoichiometric concentrations (≤equimolar ratio) was able to inhibit Aβ aggregation in a dose-dependent manner at each aggregation stage, as evidenced by (i) the increase of lag time from 9 h to time beyond machine detection limit (*i.e.*, complete inhibition), (ii) the decrease of aggregation rate during the growth phase, and (iii) the significant reduction in final ThT intensity at the equilibrium phase (Figure 1b). Specifically, ThT data in Figure 1c,d showed that 1−5 μM of PG-1 was sufficient to completely inhibit Aβ fibril formation with a low ThT intensity of −1.2−1.2% and a low fibrillization rate of 1.9−2.0 h^{-1}. Even at a very low concentration of 0.1−0.8 μM, PG-1 can still greatly reduce the Aβ fibrils by decreasing the ThT signals by 29−44% and fibrillization rate by 50−69%. In addition, from a morphological viewpoint, the AFM images (Figures 1e and S1) also showed that the co-incubation of Aβ and PG-1 exhibited much less fibrillar aggregates than that in pure Aβ samples at each aggregation stage, confirming that PG-1 indeed reduces the formation of the Aβ fibrils. Quantitatively, at 48 h, as compared to pure Aβ fibrils with an average height/length of 16/1453 nm, the introduction of PG-1 to freshly prepared Aβ solutions significantly abolished the formation of amyloid fibrils, instead formed less and short fibrils with an average height/length of 12/735 nm at PG-1 of 0.5 μM, or very few dispersed spherical particles at PG-1 of 5 μM.

To better understand the possible inhibitory pathways of Aβ aggregation by PG-1, we further examined the secondary structural transitions of Aβ (20 μM) in the absence and presence of PG-1 (0.5−5 μM) (*i.e.*, a molar ratio of Aβ/PG-1 = 1:0.025−1:0.25) using circular dichroism (CD) (Figures 1f and S2). At the beginning of aggregation (0 h), all the samples displayed a broad negative peak at ∼198 nm, indicating a predominant random coil structure for all the samples. As the aggregation proceeded, Aβ alone followed a typical structural transition from a random coil (∼198 nm) to β-sheet-rich structure (two characteristic peaks at ∼195 and ∼215 nm), finally leading to 45.5% of random coil, 0.1% of α-helix, and 54.4% of β-sheet after 48 h. In sharp contrast, the co-incubated Aβ-PG-1 samples delayed their secondary structure transition depending on Aβ/PG-1 molar ratios. This was evidenced by few β-sheet structures at Aβ/PG-1 = 1:0.025 or random coil-

https://doi.org/10.1021/acschemneuro.3c00293
ACS Chem. Neurosci. 2023, 14, 3143−3155

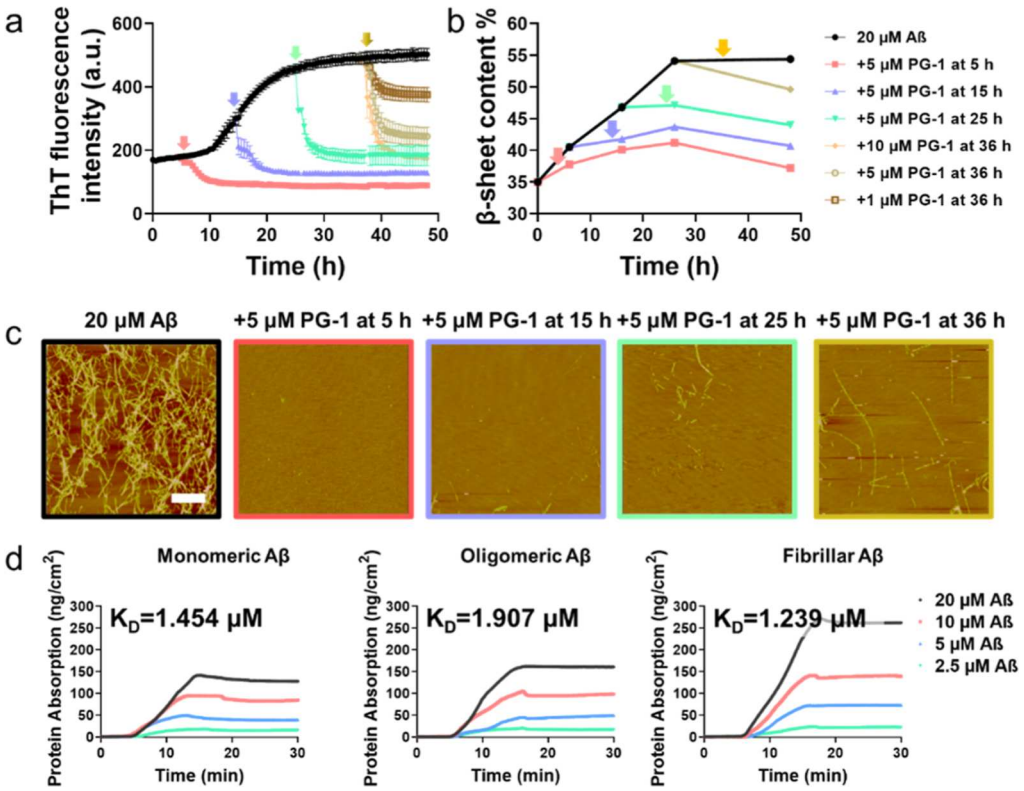

Figure 2. Cross-seeding of PG-1 with different Aβ seeds. (a) Time-dependent ThT fluorescence curves and (b) β-sheet structure changes before and after adding PG-1 (1−10 μM) to Aβ (20 μM) seeds preformed at the lag, growth, and equilibrium phases. (c) Representative AFM images of adding PG-1 (5 μM) to Aβ seeds (20 μM) preformed at the 5 h-lag-phase (pink), 15 h-early-growth-phase (blue), 25 h-late-growth-phase (green), and 36 h-equilibrium-phase (gold). The scale bars are 1 μm. (d) SPR sensorgrams show the binding amount and affinity of PG-1 to freshly prepared Aβ, oligomeric Aβ, and fibrillar Aβ at different concentrations.

dominated structures at Aβ/PG-1 = 1:0.25 after 48 h incubation. Quantitively, the secondary structure distributions calculated from CD spectra revealed that the presence of PG-1 reduced β-sheet structures by 7.9−18% but increased random coils by 4.7−16.7%. Collective data from ThT, AFM, and CD analyses suggest that the cross-seeding of PG-1 with Aβ inhibits amyloid fibrillization, and such cross-seeding-induced inhibition mainly stems from interfering with or slowing down the secondary structure transition of Aβ monomers to β-sheet-rich structures.

2.2. Cross-seeding of PG-1 with Different Aβ Seeds Modulates Amyloid Aggregation Pathways. In addition to the cross-seeding of PG-1 with Aβ monomers, we further examined the cross-seeding possibilities between non-amyloidogenic PG-1 (1−10 μM) and different Aβ (20 μM) seeds. The aggregation process of Aβ was demonstrated through the ThT profiles in Figure 1b, which clearly depicted the transition from monomers to oligomers and then to fibrils. To capture the different stages of this process, specific timepoints were selected as the incubation time. This method has been widely utilized in numerous projects within our research group, ensuring the reliable characterization of Aβ aggregation dynamics.[3,47] Specifically, different aggregation stages, including Aβ seeds from 5 h of lag phase, 15 h of growth phase, 25 h of early equilibrium phase, and 36 h of later equilibrium phase, were selected. ThT kinetics curves in Figure 2a clearly show that the addition of PG-1 to different preformed Aβ seeds still produced strong inhibition effect on Aβ aggregation, as evidenced by the sudden drop of ThT signals at the time point of Aβ addition. Quantitively, after comparing ThT data before and after adding PG-1 to 5-, 15-, and 25 h-preformed Aβ seeds, PG-1 dramatically reduced final Aβ fibrillization by 124.4% (red line), 112.3% (blue line), and 96.1% (green line), respectively. More importantly, PG-1 of different concentrations can even break down extremely stable Aβ fibrils to some extent,[48] *i.e.*, at the Aβ/PG-1 molar ratios of 1:0.05, 1:0.25, and 1:0.5, PG-1 reduced the amount of preformed Aβ fibrils by 38.3% (brown line), 77.7% (gold line), and 98.8% (orange line), respectively.

Additional cross-seeding experiments were conducted using AFM and far-UV CD spectroscopy to confirm the effect of PG-1-induced inhibition on different Aβ seeds from the perspective of secondary structure and morphological changes. As shown in Figure 2c, the addition of PG-1 (5 μM) into 5 h- (red box), 15 h- (blue box), and 25 h- (green box) pre-incubated Aβ seeds (20 μM) resulted in fewer and shorter fibrils and/or small spherical aggregates. The disaggregation ability of PG-1 became more pronounced, especially by breaking down Aβ fibrils formed at 36 h into some truncated fibrils with a length of ∼117 nm and small spherical particles of 20−50 nm. CD spectra in Figure 2b also showed that after adding 5 μM PG-1 to 5, 15, 25, and 36 h-Aβ seeds, β-sheet content was decreased to 41.2, 43.7, 47.1, and 54.1% of at 26 h (as compared to 54.1% for pure Aβ) and continuously decreased to 37.2, 40.7, 44.0, and 49.6% at 48 h (as compared to 54.4% for pure Aβ). Such reduction in β-structure content by PG-1 was also reflected by reduced peak intensities at 195 and 215 nm (Figure S3). Especially, the disaggregation ability of PG-1 enables it to act as a "β-sheet breaker" to reverse

https://doi.org/10.1021/acschemneuro.3c00293
ACS Chem. Neurosci. 2023, 14, 3143−3155

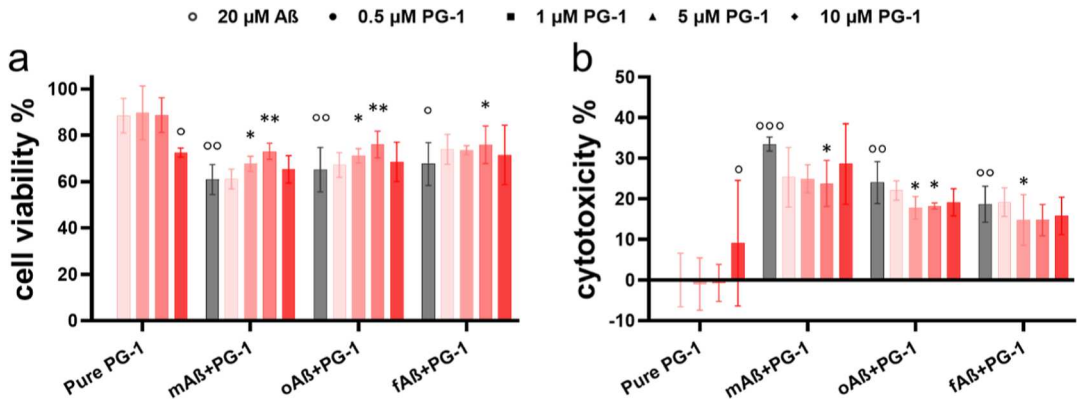

Figure 3. Cytoprotective effect of PG-1 on Aβ-induced SH-SY5Y neuron cells. Dose-dependent protection effect of PG-1 on Aβ-induced (a) cell toxicity by MTT assay and (b) cell membrane disruption by LDH assay. SH-SY5Y neuron cells were incubated with different Aβ (20 μM) seeds for 24 h in the absence (gray bar) or presence (colored bar) of 0.5−10 μM PG-1. PG-1 and Aβ-treated cells were normalized by untreated cells, which served as the positive control (representing 100% MTT reduction and 0% LDH activity), and cells treated with lysis buffer, which served as the negative control (representing 100% LDH activity). All data presented are the mean ± standard deviation (s.d.) of three independent experiments. Statistical analysis (n = 3) was conducted for cells treated with PG-1 or Aβ alone relative to control (°, $p < 0.05$; °°, $p < 0.01$; °°°, $p < 0.001$), and cells treated with both PG-1 and Aβ relative to cells treated with Aβ alone (*, $p < 0.05$; **, $p < 0.01$; and ***, $p < 0.001$).

preformed and pathologically associated Aβ aggregates, which could be used as a promising strategy for the treatment of AD.

Hypothetically, such strong inhibition/disaggregation property of PG-1 mainly stems from their strong interactions with Aβ to competitively reduce Aβ−Aβ interactions, thereby inhibiting Aβ aggregation and breaking down preformed Aβ aggregates. To test this hypothesis, we measured the binding affinity of PG-1 to different Aβ seeds using surface plasmon resonance (SPR).[49] Briefly, freshly dissolved PG-1 was first covalently immobilized on an SPR chip surface *via* direct amine-coupling. Then, Aβ monomers, oligomers, and fibrils obtained by incubating for 0 h (freshly prepared), 15 h (half time), and 36 h (saturated phase) were diluted into different concentrations and separately flowed through the PG-1-anchored SPR chips, followed by a PBS buffer solution to wash off any weakly bound Aβ on the PG-1-coated surface. As a result, the total amount of strongly adsorbed Aβ seeds on the PG-1-coated surface is determined by a wavelength shift between the two baselines before injecting amyloid solution and after injecting PBS buffer solution. A quick glance at SPR sensorgrams in Figure 2d shows that the surface-immobilized PG-1 had a general, strong binding capacity for all of three Aβ seeds in a concentration-dependent manner, *i.e.*, as the Aβ concentration increased from 2.5 to 20 μM, its adsorption amount on PG-1-coated surfaces increased from 17 to 141 ng/cm^2 for Aβ monomers, from 20 to 160 ng/cm^2 for Aβ oligomers, and from 23 to 271 ng/cm^2 for Aβ fibrils. Such cross-species interactions between PG-1 and Aβ seeds are strong enough that Aβ cannot be easily washed off by PBS solution, as evidenced by only very small amounts of Aβ being washed away (*i.e.*, 1−14 ng/cm^2 for Aβ monomers, 0−6 ng/cm^2 for Aβ oligomers, and 1−8 ng/cm^2 for Aβ fibrils). Further kinetic analysis of SPR sensorgrams determined that PG-1 had the dissociation constants of 1.454 μM for Aβ monomers, 1.907 μM for Aβ oligomers, and 1.239 μM for Aβ fibrils (Figure S4). Taken together, PG-1 strongly prefers to interact with the Aβ seeds with predominant β-structures, and this is evidenced by the descending order of binding affinity of PG-1 to Aβ seeds: Aβ fibrils > Aβ oligomers > Aβ monomers, further demonstrating that the strong binding affinity between PG-1 to Aβ seeds is mainly driven by the interactions of conformationally similar β-structures.

2.3. Cross-seeding of PG-1 with Aβ Rescues Amyloid-Mediated Cytotoxicity. Recent studies showed a parallel between channel-forming Aβ peptides and channel-forming PG-1 based on a common β-sheet structure, in which toxic β-sheet PG-1 channels have a subunit organization motif that was very similar to that of Aβ channels.[28] While both PG-1 and Aβ exhibit similar toxicity to their respective target cells, our cross-seeding results showed that PG-1 enables inhibition of Aβ aggregation and even break down preformed Aβ fibrils *via* cross-seeding. Here, we continued to investigate whether such cross-seeding of PG-1 with Aβ seeds still occurs in the presence of cells, if so, how does it affect cell cytotoxicity? To this end, we applied MTT (Figure 3a) and LDH (Figure 3b) assays to study cell viability and cytotoxicity by co-incubating PG-1 (0.5−10 μM) with freshly prepared (monomers), 15 h (oligomers), and 36 h (fibrils) incubated Aβ solutions (20 μM) in the presence of SH-SY5Y neuron cells for 24 h. For comparison, all Aβ or PG-1-treated cell viability and toxicity data were normalized by the untreated cell group (as positive control) and the lysis buffer-treated cell group (as negative control), *i.e.*, 100% MTT reduction and 0% LDH activity. As controls, three different Aβ seeds exhibited high toxicity to cells, as evidenced by 65−70% cell viability and 9−24% cell apoptosis upon 24 h of incubation with cells (gray bars in Figure 3). It is not surprising that older Aβ seeds induced lesser cell cytotoxicity than the younger ones because the younger Aβ seeds undergo a more complete misfolding and aggregation process with cells. In sharp contrast, pure PG-1 of different concentrations from 0.5 to 5 μM exhibited 88%−90% cell viability and 0.02−0.03% cytotoxicity, indicating almost non-toxicity to SH-SY5Y cells, but PG-1 at a higher concentration of 10 μM showed little toxicity to SH-SY5Y cells, with 73% cell viability and 9% cytotoxicity.

When co-incubating PG-1 with Aβ-treated SH-SY5Y cells, PG-1 exhibited a dose-dependent cytoprotective effect. It was evidenced by the increased cell viability and decreased cytotoxicity as compared to the corresponding Aβ seeds systems alone. Specifically, for the PG-1-Aβ monomer system, increase of PG-1 concentrations from 0.5−5 μM rescued the

https://doi.org/10.1021/acschemneuro.3c00293
ACS Chem. Neurosci. 2023, 14, 3143−3155

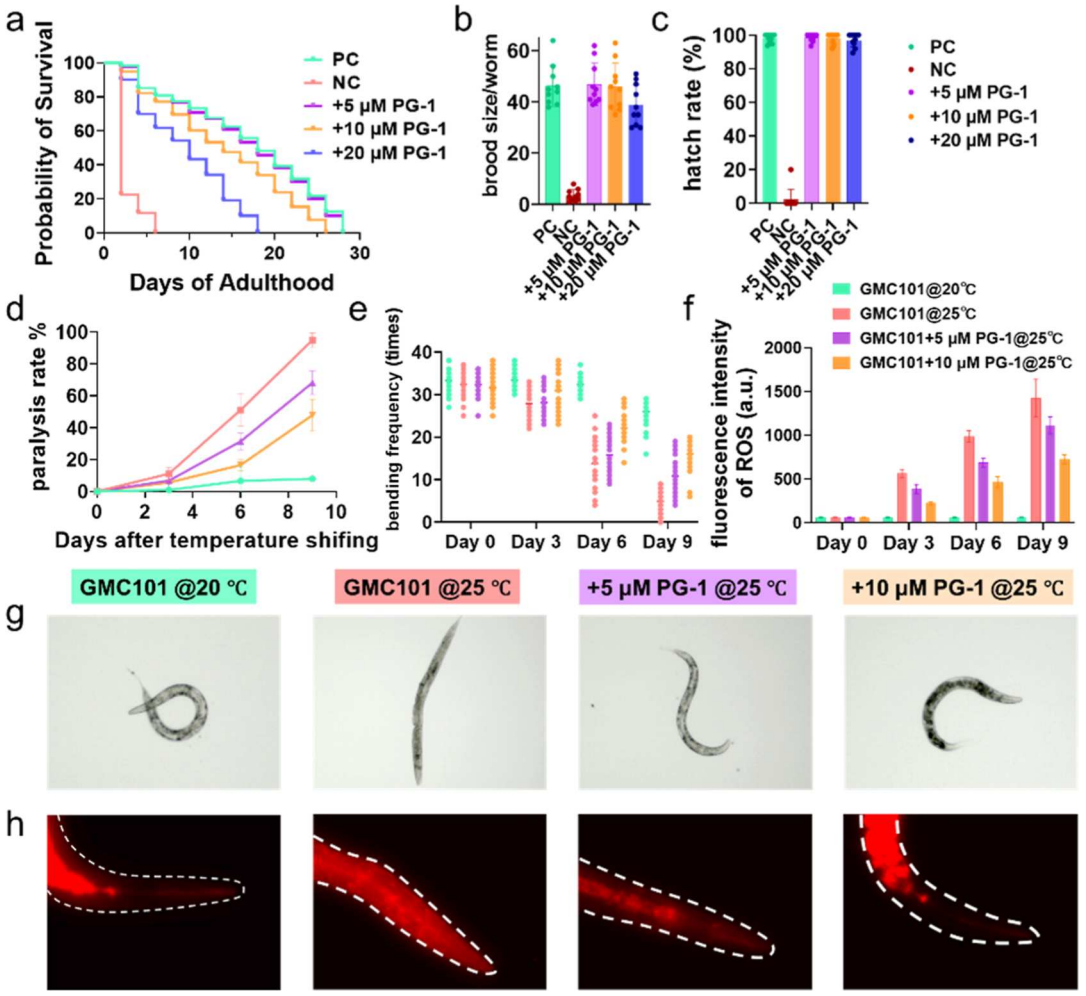

Figure 4. PG-1 alleviates Aβ-induced nematode paralysis in transgenic GMC101 *C. elegans*. (a) Lifespan probability, (b) brood size, and (c) hatching rate of wild-type N2 worms treated with S-complete buffer (green), 0.5 M NaOH (red), 5 μM PG-1 (purple), 10 μM PG-1 (orange), and 20 μM PG-1 (blue). A *t*-test was performed to analyze the data from worms treated with PG-1 compared to the positive control (*i.e.*, untreated worm groups, $n = 10$). (*$p < 0.05$, **$p < 0.01$, ***$p < 0.005$, and ****$p < 0.001$). Paralysis assays for characterizing the (d) paralysis rate, (e) bending frequency, (f) ROS intensity, (g) real-time mobility image in liquid medium, and (h) *in vivo* NIAD-4 staining of age-synchronized GMC101 worms treated with 5 (purple) or 10 μM (orange) PG-1 at 25 °C (red) for 9 days. As a comparison, S-complete buffer-treated GMC101 worms cultured at 20 °C (green) and 25 °C (red) were used as positive and negative controls, respectively. Scale bars are 100 μm.

SH-SY5Y cells from Aβ-induced toxicity by increasing the cell viability by 0.3−20% and reducing the cell cytotoxicity by 24−29%, respectively. However, doubling the concentration of Aβ to 10 μM led to further reduction of cell toxicity to a large extent, mainly due to the competition between the cytoprotection induced by PG-1 inhibition and the cellular damage caused by Aβ and PG-1, especially at higher concentrations. Quantitively, PG-1 of 10 μM improved cell viability by 7.3% and decreased cell toxicity by 15% when co-incubating with Aβ and cells. Such a "double-edged sword" effect of PG-1 was also verified in both the PG-1-Aβ oligomer systems and PG-1-Aβ fibril systems. Evidently, as the PG-1 concentration increased from 0.5 to 5 μM, PG-1 can attenuate Aβ oligomer-induced toxicity by increasing the cell viability by 3−17% and decreasing the cell toxicity 8−26%. A similar cytoprotective effect of PG-1 was found for the PG-1-Aβ fibril systems by increasing the cell viability by 9−12% and reducing cytotoxicity by 3−21%. Notably, a higher concentration of PG-1 (10 μM) slightly reduced its cytoprotective effect, so that for the Aβ oligomer and fibril systems, the cell viability only increased by 5−6%, while the cell toxicity reduced by 15−20%.

Together with the cross-seeding results between PG-1 and Aβ from ThT, AFM, and CD, PG-1 has been shown to inhibit Aβ aggregation, thereby reducing the formation of toxic Aβ species that can disrupt cell membranes. By preventing the accumulation of toxic aggregates, PG-1 may indirectly protect cell membranes from the detrimental effects of Aβ. Second, the formation of PG-1−Aβ heterocomplexes, instead of Aβ−Aβ homo-aggregates, may contribute to the reduced cytotoxicity observed. The interaction between PG-1 and Aβ could lead to the sequestration or neutralization of toxic Aβ species, preventing their interaction with cell membranes and subsequent membrane disruption. While these hypotheses provide a plausible explanation for the observed reduction in cytotoxicity, the precise binding mechanism and specific binding sites involved require further investigation. Computational simulations and experimental studies focusing on protein−membrane interactions may shed more light on the detailed mechanisms of PG-1's protective effect against Aβ-induced cytotoxicity. We encourage further exploration in this area to gain a more comprehensive understanding of the binding and interaction between PG-1 and Aβ.

https://doi.org/10.1021/acschemneuro.3c00293
ACS Chem. Neurosci. 2023, 14, 3143−3155

2.4. Cross-seeding of PG-1 with Aβ Inhibits Aβ-Mediated Dysfunction in Nematode. To extend this study from *in vitro* cells to *in vivo* worms, we used the nematode *Caenorhabditis elegans* as an *in vivo* biological model to test the protective ability of PG-1 against Aβ-induced toxicity because an *in vivo* model can take into account more complex factors, including genotype modification, endogenously tagged loci, and disease-associated mutants. For comparison, we employed two types of *C. elegans* strains including (i) wild-type *C. elegans* N2 strain, without genetic modifications, for testing the toxicity of PG-1 itself to *C. elegans* (Figure 4a−c) and (ii) transgenic *C. elegans* GMC101 strain that expresses human $A\beta_{1-42}$ in body wall muscle cells for examining the beneficial effect of PG-1 on AD prevention (Figure 4d−h). As shown in Figure 4a, 0.5 mM NaOH-treated worms (as negative control, NC, red line) induced 100% worms' death after 6 days, while S-complete buffer-treated worms (as positive control, PC, green line) underwent a normal lifecycle and survived for 28 days. For comparison, the PG-1-treated N2 worms exhibited self-toxicity in a concentration-dependent manner. Specifically, the survival curve of 5 μM PG-1 (purple line) almost overlapped with the positive control group, indicating little or no toxicity of PG-1 at this concentration. Further increase of PG-1 concentration to 10 μM (orange line) and 20 μM (blue line) led to a gradual decrease of survival rate, ultimately reducing their lifespan to 18 and 26 days, respectively. In addition, we counted the number of eggs (brood size, Figure 4b) and the hatchability of the eggs (Figure 4c) laid by a single nematode during the first 24 h of adult life in the presence of different concentrations of PG-1. As controls, the positive and negative control groups laid 46.3 and 3.5 eggs, respectively, and the hatching rates were 98 and 2% at the L1-stage, respectively. Dietary supplementation with PG-1 from 5 to 20 μM led to reduction in worm brood size of 46.9−38.9 and worm hatchability of 98−97%. Combined with worm lifespan results in Figure 4a, PG-1 showed dose-dependent toxicity to normal worms.

Given the apparent toxicity of 20 μM PG-1 to worms, only 5−10 μM PG-1 was chosen to further investigate how PG-1 supplementation affects Aβ toxicity-induced progression of worm paralysis by using a transgenic, age-synchronized nematode GMC101 strain. In a GMC 101 worm model, $A\beta_{42}$ is expressed in body wall muscle cells, where it forms aggregates and induces severe age-progressive paralysis when the temperature upshifts from 20 to 25 °C.[50] In this study, GMC101 worms were first cultured at 20 °C without PG-1 administration, and since there was no Aβ expression in these worms at 20 °C, they were considered as the control group. As shown in the green data from Figure 4d−h, the untreated GMC101 worms cultured at 20 °C display normal activities, including (i) a low paralysis rate of 8% (Figure 4d); (ii) a normal bending frequency of 26 times per min (Figure 4e); (iii) low reactive oxidative species (ROS) fluorescence intensity of 61 a.u (Figure 4f); (iv) free bending degree from 90 to −90° (Figure 4g); and (v) no accumulation of Aβ aggregates in the head region (red fluorescence, Figure 4h).

For comparison, GMC101 worms cultured at 25 °C in the absence (red) and presence of 5−10 μM PG-1 (purple and orange) exhibited significant age-progressive paralysis symptoms. Specifically, the untreated worms cultured at 25 °C showed a typical time-dependent, progressive paralysis. By touching the worms on days 3, 6, and 9 after the temperature change to 25 °C, 11, 51, and 95% of the worms were paralyzed (*i.e.*, no responsive reaction). However, during the same 9 day culture, the paralysis rate of worms treated with 5 or 10 μM PG-1 was greatly reduced to 68 or 48% (Figure 4d). The frequency of worm body bending, indicative of the muscle cell status, reconfirmed that PG-1 can rescue Aβ-mediated dysfunction in *C. elegans* models. In the absence of PG-1, the frequency of body bending in GMC101 worms decreased after only 6 days, whereas a similar bending decrease occurred after 9 days for worms treated with 10 μM PG-1. Quantitively, GMC101 worms treated with 0, 5, and 10 μM PG-1 exhibited 27, 28, and 31 bends on day 3, 14, 16, and 22 bends on day 6, and 5, 11, and 16 bends on day 9 (Figure 4e). On the other hand, excessive production of ROS, which is also considered to be a harmful substance, exacerbates Aβ aggregation-induced AD progression. As shown in Figure 4f, on each test day (*i.e.*, days 3, 6, and 9), GMC101 worms administered with 5−10 μM PG-1 induced lower ROS intensity than that in untreated worms, and this reduction in ROS was dose-dependent. As compared with untreated-GMC101 worms, GMC101 worms treated with 10 μM PG-1 significantly suppressed the production of ROS by 61, 53, and 49% at days 3, 6, and 9, respectively (Figure 4f).

Consistent with the abovementioned differences between PG-1 treated and untreated GMC101 worms incubated in 25 °C, microscopy images (Figure 4g) and fluorescence images of Aβ aggregates monitored using Aβ-specific dye NIAD-4 (Figure 4h) showed obvious differences between normally active worms treated with PG-1 and paralyzed worms without any treatment. Specifically, the untreated worm (red) cultured in 25 °C (i) displayed rigid "rod-like" shape in liquid medium; (ii) largely restricted its bending; and (iii) showed massive Aβ deposition in its head region (red fluorescence of $1.6*10^7$ a.u.). In contrast, the worms treated with 5 PG-1 (purple) and 10 μM (orange) exhibited a smooth body shape, with varying degrees of curvature and Aβ deposition. When supplemented with 10 μM PG-1, the maximum bending degree of the GMC101 worms became even more pronounced, which was very close to the normal state of untreated worms incubated at 20 °C. Moreover, as compared with 5 μM PG-1-treated worms that emitted an Aβ-induced fluorescence intensity of $9.4*10^6$ a.u., almost no Aβ aggregates were detected in worms treated with 10 μM PG-1. Collective results demonstrate that PG-1 can inhibit Aβ aggregation and deposition in transgenic AD worms.

2.5. Cross-seeding of PG-1 with Aβ Retains Antimicrobial Properties. Given the facts that (i) PG-1 has an intrinsic antimicrobial function; (ii) Aβ has been identified as a new antimicrobial agent against bacteria, fungi, and viruses; and (iii) antimicrobial and amyloid peptides share some a commonality that could kill their target cells by disrupting their cell membranes, it will be interesting to study whether the antimicrobial property of PG-1 and Aβ can be preserved after the cross-seeding of PG-1 and Aβ. To this end, we examined the antimicrobial activity of PG-1, Aβ, and their hetero-complexes using Gram-negative bacterial strains of *Escherichia coli* (*E. coli*) and *P. aeruginosa* (P.A.) and Gram-positive bacterial strains of *Staphylococcus aureus* (S.A.) and *S. epidermidis* (S.E.). As shown in the inhibitory concentration map in Figures S5a and S6, PG-1 exhibits broad-spectrum antibacterial properties over a wide concentration range (0.5−80 μM) against four different bacterial strains, in descending order of antibacterial efficacy: *E. coli* ≈ S.E. > S.A. ≈ P.A. Especially, 40 μM PG-1 can completely inhibit the growth of *E. coli* and S.E. Differently, pure Aβ had the much less

https://doi.org/10.1021/acschemneuro.3c00293
ACS Chem. Neurosci. 2023, 14, 3143−3155

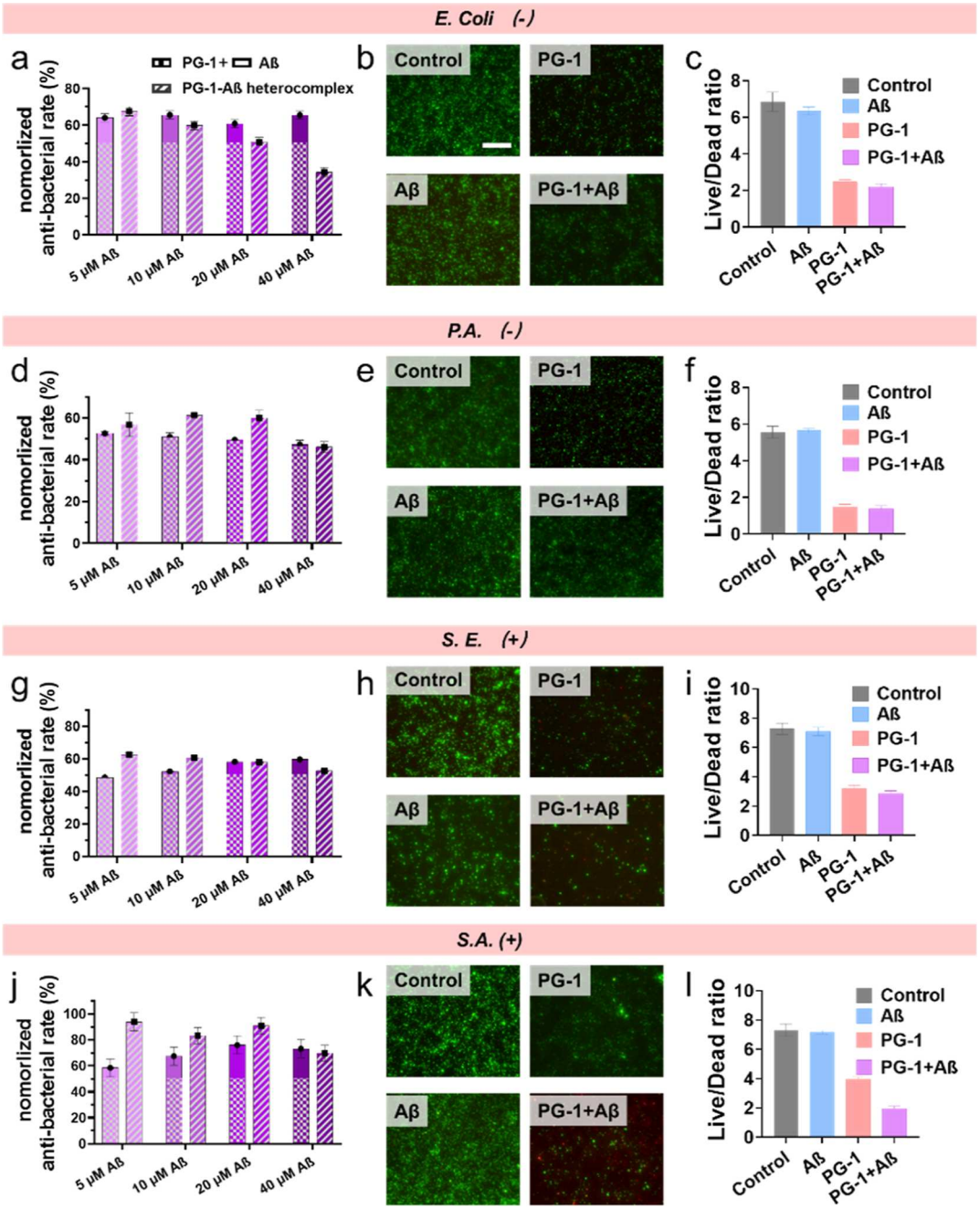

Figure 5. PG-1−Aβ complexes retain a broad-spectrum antimicrobial property. Antimicrobial activity of PG-1 at IC_{50} (checked bars), 5−40 μM Aβ (solid bars), and PG-1−Aβ complexes (shadowed bars) against Gram-negative (a−c) *E. Coli* and (d−f) P.A. and Gram-positive (g−i) S.E. and (j−l) S.A. PG-1- and Aβ-treated cells were normalized to untreated cells (control, 0% antibacterial rate). The presented data represent the mean ± standard deviation (SD) of three independent experiments. Antimicrobial activity was quantified by (a,d,g,j) OD_{600} for final bacterial density, (b,e,h,k) representative fluorescence microscopy images, and (c,f,i,l) bacterial live/dead ratios. The scale bars in live/dead images are 180 μM.

antimicrobial ability than pure PG-1 at the same concentration, with a lower inhibition efficiency of 14−26% against the four bacterial strains over the same incubation period (Figure S5b).

Next, we tested the antimicrobial activity of co-assemblies of PG-1 and Aβ (shadowed bars in Figure 5a,d,g,j, named as PG-1-$A\beta_{5\text{-}40,\text{concnetration}}$ complexes) as compared to that of pure PG-1(ticked bars in Figure 5a,d,g,j) and pure Aβ (blank bars in Figure 5a,d,g,j) (named as PG-1 + $A\beta_{5\text{-}40,\text{concnetration}}$). Considering the different killing ability of PG-1 to different bacterial strains, here, we used the inhibitory concentration (IC_{50}) of PG-1 for specific bacteria strains, that is, 14, 46, 5, and 49 μM for *E. coli*, P.A., S.E., and S.A, respectively, where IC50 values for specific bacterial strains were obtained from three replicated tests in Figure S7. With the fixed IC50 of PG-1, Aβ concentrations were varied from 5 to 20 μM to test any concentration-dependent antimicrobial effects. As a result, the PG-1-Aβ complexes generally exhibited a comparable or even higher antimicrobial efficiency than PG-1 + Aβ samples, especially at lower Aβ concentrations of 5−20 μM. Evidently, this enhanced antimicrobial property became more pronounced in S.A. and P.A. strains, in which PG-1-$A\beta_{5-20}$ complexes (83−94% for S.A. and 57−61% for P.A.) had

https://doi.org/10.1021/acschemneuro.3c00293
ACS Chem. Neurosci. 2023, 14, 3143−3155

higher antibacterial efficiency than PG-1 + $A\beta_{5\text{-}20}$ samples (58−76% S.A. and 50−53% for P.A.). Doubling $A\beta$ concentration to 40 μM slightly reduced the antimicrobial activities of PG-1-$A\beta_{40}$ complexes from 47−73 to 46−70%, which may be due to the excessive $A\beta$ affecting the interaction between PG-1−$A\beta$ complexes and bacteria (Figure 5d,j). Due to the relatively poor antibacterial efficiency of pure PG-1 and $A\beta$ against S.A. and P.A. strains (Figures S5,S6), the enhanced antibacterial ability of the PG-1−$A\beta$ complexes should originate from their cross-species interactions. Similar trend was also observed in the case of S.E., *i.e.*, as compared to PG-1 + $A\beta_{5-40}$ samples to kill 49−60% S.E., (i) PG-1-$A\beta_{5-10}$ complexes exhibited a higher anti-bacteria capacity to kill 61−62% S.E.; (ii) PG-1-$A\beta_{20}$ complexes showed a comparable antimicrobial capacity to kill 58% S.E.; and (iii) PG-1-$A\beta_{40}$ complexes had an inferior anti-bacterial capacity to kill 53% S.E (Figure 5g). In contrast, all PG-1−$A\beta$ complexes presented a comparable or inferior antimicrobial activity against *E. coli* to their corresponding PG-1 + $A\beta$ samples, which may be due to the lower sensitivity of PG-1−$A\beta$ complexes to specific *E. coli* (Figure 5a).

Additionally, we monitored the bacterial membrane integrity to distinguish the live (green) bacteria and dead (red) bacteria in the presence of PG-1 and $A\beta$ using live/dead staining assay. As shown in Figure 5b,e,h,k, all bacterial strains without any treatment (*i.e.*, the control groups) displayed massive green fluorescence, an indicator of normal bacterial growth. In the case of bacterial strains treated with pure $A\beta$, it can be clearly seen that 5 μM $A\beta$ had little cytotoxicity to the bacteria, as indicated by no obvious changes in the green fluorescent signals and live/dead ratios of 5.6−7.2 (*i.e.*, green/red ratio), both of which were similar to those in the control samples (live/dead ratios = 5.8−7.3, Figure 5c,f,i,l). Oppositely, pure PG-1 caused a high number of dead cells by reducing bacterial density (*i.e.*, weak green fluorescent signal) and bacterial live/dead ratio by 45−73%. When PG-1−$A\beta$ complexes were co-incubated with bacterial strains, it still produced strong red fluorescent signals, which are an indicator of bacterial death due to membrane damage. Quantitively, the live/dead ratios of *E.coli*, P.A., S.E., and S.A. were reduced to 2.2, 1.4, 2.9, and 2.0, respectively, further confirming that PG-1−$A\beta$ complexes are able to preserve antibacterial property.

3. CONCLUSIONS

$A\beta$ aggregation and microbial infection are the two common pathological causes of AD. Conceptually, the repurposing of antibacterial peptides with intrinsic antimicrobial activity as amyloid inhibitors is a plausible strategy to simultaneously achieve anti-neuroinflammation and anti-amyloid functions. Here, we demonstrated this repurposing strategy by discovering PG-1 as the $A\beta$ inhibitor and microbicide. As an $A\beta$ inhibitor, collective aggregation data from ThT, CD, and AFM showed that PG-1 was able to cross-interact with different $A\beta$ seeds including monomers, oligomers, and fibrils to inhibit $A\beta$ aggregation *via* different inhibition pathways. The first $A\beta$ inhibition pathway by PG-1 is to interfere with the secondary structural transition of $A\beta$ monomers and oligomers toward $A\beta$ fibrils, leading to almost complete inhibition of $A\beta$ fibrillization and 18% of β-structure reduction even at 5 μM. The second inhibition pathway is the breakdown of mature $A\beta$ fibrils into small aggregates. SPR results further revealed the high binding affinity of PG-1 with different $A\beta$ seeds, as evidenced by dissociation constants of K = 1.24−1.90 μM. At the cellular level, MTT and live/dead cell assays showed that PG-1 was able to rescue the SH-SY5Y cells from $A\beta$-induced cytotoxicity by increasing cell viability by ∼0.3−20% and reducing cytotoxicity by ∼3−29%. *In vivo* wild-type and transgenic *C. elegans* worm models showed that PG-1 can attenuate $A\beta$-induced AD-like phenotype in worms, and this was demonstrated by 27−47% reduction in worm paralysis, 120−220% increase in worm bending frequency, 41−100% reduction of $A\beta$ plaques in worm head, and 22−49% reduction in ROS production. Finally, when PG-1 cross-seeded with $A\beta$, the PG-1−$A\beta$ complexes still maintained similar or even better antibacterial activities against four different Gram-positive and Gram-negative bacteria as compared to pure PG-1.

Overall, this work introduces a new model that not only reconciles the "amyloid cascade hypothesis" and the "microbial infection hypothesis" but also unravels the functional and structural connections between antimicrobial peptides and amyloid proteins. By capitalizing on the inherent capabilities of antimicrobial peptides to combat bacteria and inhibit amyloid formation, our approach offers a unique opportunity to simultaneously target both the pathways of amyloid aggregation and microbial infection. Additionally, our findings shed light on the functional and structural resemblances between antimicrobial peptides and amyloid proteins, providing valuable insights into the underlying mechanisms of amyloid diseases and paving the way for the development of more efficacious treatment strategies.

4. METHODS

4.1. Reagents. Amyloid beta ($A\beta_{1-42}$, ≥95%) was purchased from CPC Scientific (Sunnyvale, CA), and protegrin-1 (PG-1, ≥95%) was synthesized by Genscript. Thioflavin T (ThT, 98%), dimethyl sulfoxide (DMSO, ≥99.9%), and 1,1,1,3,3,3-hexafluoro-2-propanol (HFIP, ≥99.9%) were obtained from Sigma-Aldrich (St. Louis, MO). All the remaining chemicals used were of the highest grade available.

4.2. Peptide Purification and Preparation. $A\beta$ and PG-1 were stored in −20 °C before use. To obtain the monomeric peptides, all pre-packaged peptides (*i.e.*, 1 mg of PG-1 and $A\beta$) were redissolved in 1 mL of HFIP and incubated at room temperature for 2 h. Subsequently, peptides underwent 30 min of sonication in an ice bath and 30 min of centrifugation (14,000 rpm, 4 °C). The 80% supernatant was stored at −80 °C. Unless specified otherwise, all the peptides were initially solubilized in 10 mM NaOH and then further dissolved in various buffers to achieve the desired concentration.

4.3. Thioflavin T Fluorescence Assay. The aggregation of $A\beta$ was tracked using a SpectraMax M3 microplate reader (Molecular Devices, CA, USA). Measurements were taken in kinetic top-read mode, with an excitation wavelength of 450 nm and an emission wavelength ranging from 470 to 500 nm. ThT stock solution was prepared by dissolving ThT into Milli-Q water to a concentration of 2 mM. The stock solution was stored in a dark area at room temperature before use. The resulting stock solution was sonicated to ensure it was particle-free and then further diluted in Tris-buffer to a concentration of 10 μM. Sample preparations were performed on ice by mixing $A\beta$ with and without PG-1 (at concentrations ranging from 0.1 to 5 μM) to achieve a total test volume of 200 μL.

4.4. Circular Dichroism Spectroscopy. The transition of the secondary structure during $A\beta$ aggregation was monitored using far-ultraviolet CD spectroscopy. Here, a J-1500 spectropolarimeter (Jasco Inc., Japan) was employed for this purpose, operating in continuous scanning mode at room temperature. Samples were prepared by incubating $A\beta$/PG-1/$A\beta$-PG-1 at 37 °C in 10 mM phosphate-buffered saline (PBS, pH 7.4) for varying time periods. Subsequently, 150 μL of each sample was transferred to a 1 mm optical path length CD cuvette. The solution's spectra were recorded between 190 and 250 nm at a resolution of 0.5 nm and a scan rate of 50 nm/min. In

https://doi.org/10.1021/acschemneuro.3c00293
ACS Chem. Neurosci. 2023, 14, 3143−3155

order to eliminate background interference, the spectra were baseline-corrected by subtracting the PBS buffer spectrum. To quantitatively determine the secondary structural contents, the Beta Structure Selection (BeStSel) algorithm[51] (http://bestsel.elte.hu/) was used.

4.5. Atomic Force Microscopy. The morphological changes of Aβ aggregation mediated by PG-1 were characterized by using a Nanoscope III multimode atomic force microscope (Veeco, NY, USA). Sample was prepared by incubating Aβ with and without 0.5−5 μM PG-1 in 10 mM PBS buffer for varying time periods (*i.e.*, 6 and 24 h). Then, 20 μL of Aβ-PG-1 was deposited on a piece of cleaved mica for at least 5 min, followed by rinsing with Milli-Q water three times to ensure complete removal of any excess salt. Afterward, they were dried using an air stream and stored in a sealed container. All the images were recorded at a resolution of 256 × 256 pixels, with a typical scan rate of 1.0 Hz and a vertical tip oscillation frequency ranging from 250 to 350 kHz. Representative AFM images were acquired by scanning six distinct locations on the surface of the mica.

4.6. Surface Plasmon Resonance Spectroscopy. To perform real-time monitoring of PG-1 absorption on Aβ, a custom-built four-channel SPR sensor utilizing wavelength interrogation was employed. To prepare a dextran-modified SPR sensor chip, the clean gold surface was initially immersed in a solution of 5 mM 11-mercapto-1-undecanol in ethanol/water (8:2) for a duration of 24 h. This process resulted in the formation of a thiol-based surface. The next step involved treating the surface with epichlorohydrin (2% v/v) in 0.1 M NaOH for a period of 3 h. Subsequently, the surface was transferred to a 300 g/L dextran solution (500 kDa) in 0.1 M NaOH for 24 h, leading to the formation of carboxymethylated dextran-modified SPR chips. To finalize the preparation, the resulting surfaces were thoroughly rinsed with Milli-Q water and then immersed in a solution of 1.0 M bromoacetic acid in 2 M NaOH for 24 h. This step facilitated the creation of the dextran-modified SPR sensor chip.

To immobilize PG-1, PBS buffer was first injected through four separate channels using a peristaltic pump for a duration of 10 min to establish the baseline. To activate the SPR chips, an equal molar mixture of NHS (*N*-hydroxysuccinimide) and EDC (*N*-ethyl-*N*-(diethylaminopropyl) carbodiimide) was applied. Following the activation step, PG-1 dissolved in PBS (10 mM, pH 7.4) was introduced to the sample surface and allowed to interact for a duration of 10 min. 1 M ethanolamine HCL (pH = 8.5) was injected for another 10 min to deactivate any unreacted groups. To determine the binding affinity of PG-1 with Aβ, a serial dilution of Aβ ranging from 2.5 to 20 μM was injected into the channels of the SPR sensor using a running buffer of 10 mM PBS (pH 7.4). The flow rate during this injection was set to 5 μL/min. PBS buffer was subsequently introduced to remove any unbound Aβ. In this study, a wavelength shift of 1 nm at 750 nm on the SPR sensor indicated a surface coverage of approximately 15 ng/cm^2 of the absorbed protein. The dissociation constant (K_D) values were determined using Anabel software (http://anabel.skscience.org/). The data was fitted using a 1:1 Langmuir binding model, and the observed binding constant (kobs) was obtained using the linearization method.

4.7. Seeding Assays. For the seeding experiment, 5 μL of PG-1-NaOH mixture was added into Aβ solution pre-incubated for 5, 15, 25, and 36 h and kept to monitor aggregation curves (*i.e.*, ThT and CD test) to illustrate the cross-seeding interaction between PG-1 and Aβ seeds. Furthermore, to provide additional evidence for the primary forms of Aβ during the selected time intervals, we conducted AFM and CD analyses in our previous study.[52] For instance, the AFM images clearly demonstrated that freshly prepared Aβ monomers at 0 h exhibited minimal observable aggregates, whereas Aβ monomers at $t_{1/2}$, representing half of the maximum fibril amount, showed only a few observable aggregates. These findings were consistent with the corresponding CD spectra, which indicated the presence of characteristic random coil structures for freshly prepared Aβ monomers and less-populated β-sheet structures for Aβ monomers at $t_{1/2}$ (red boxes). Finally, Aβ fibrils at the saturated stage exhibited dense mature fibrils in AFM images and saturated β-sheet structures in CD spectra. These complementary techniques have allowed us to confidently identify and characterize the primary forms of Aβ at different stages of aggregation.

4.8. Cell Culture. Neuroblastoma cell line SH-SY5Y (ATCC CRL-2266, Manassas, VA) was used as an *in vitro* cell model to study the protection capacity of PG-1 on Aβ-induced cytotoxicity. The cells were cultured in 25 cm^2 T-flasks using a sterile-filtered mixture of ATCC-formulated Eagle's minimum essential medium (ATCC, Manassas, VA) and F12 Medium (Sigma-Aldrich, St. Louis, MO) in a 1:1 ratio. The culture medium was supplemented with 10% fetal bovine serum (ATCC, Manassas, VA) and 1% penicillin/streptomycin (ATCC, Manassas, VA). The T-flasks were then placed in a humidified incubator at 37 °C with 5% CO_2. The cells were allowed to grow until they reached approximately 80% confluence. To harvest the cells, a 0.25% Trypsin−EDTA (1×) solution (Lonza, Walkersville, MD) was used, and the cells were subsequently seeded into 96-well plates (2 × 10^5 per well).

4.9. Cell Assays. 3-(4,5-Dimethylthiazole-2-yl)-2,5-diphenyltetrazolium bromide (MTT) reduction assay was used to test the cellular metabolic activity to serve as an indicator of cell viability, while lactate dehydrogenase (LDH) assay was used to test cell membrane leakage to serve as an indicator of cytotoxicity.

The 96-well plate seeded with SH-SY5Y cells was incubated for 24 h to ensure cell attachment. Afterward, the cell culture medium was replaced with fresh medium containing Aβ, PG-1, or Aβ-PG-1 solutions. The cells were then cultured for an additional 24 h at 37 °C with 5% CO_2 in a humidified incubator. Subsequently, to the setup spontaneous/maximum LDH activity and maximum LDH activity controls, 10 μL of sterile, ultrapure water or 10× Lysis buffer was added to different wells and incubated for 45 min, followed by transferring 50 μL of supernate medium from each well to a clean 96-well plate. 50 μL of reaction mixture was then added to each well, mixed well, and incubated for another 30 min. Finally, 50 μL of a stop solution was added to each well, and the absorbance was measured at 490 and 680 nm using a SpectraMax M3 microplate reader. To determine the LDH activity, the background absorbance value at 680 nm was subtracted from the absorbance value at 490 nm before calculating the percentage of cytotoxicity.

The following formula was used for the calculation of % cytotoxicity

$$\%\ \text{cytotoxicity} = \left(\frac{\text{PG} - \text{1 treated LDH activity} - \text{spontaneous LDH activity}}{\text{maximum LDH activity} - \text{spontaneous LDH activity}}\right) \times 100\%$$

The drug-treated cells were used for MTT assay. In short, the cell culture medium was removed, and the cells were labeled with a 0.5 mg/mL MTT culture medium solution at 37 °C for 4 h. Following this, the formazan crystals were dissolved in dimethyl sulfoxide. The absorbance value was measured at 540 nm using a SpectraMax M3 microplate reader, and the cell viability was determined by calculating the percentage of MTT reduction compared to that in the untreated cells. For both MTT and LDH, each sample was counted in triplicate and reported as mean ± SD.

The representative images of the live and dead cells were obtained using a LIVE/DEAD Viability/Cytotoxicity Kit (L3224, Invitrogen) and captured using a fluorescence microscope (Echo RVL2-K) to visualize the live and dead cells. The fluorescence intensity of the respective images was quantified using ImageJ software, with a sample size of n = 3.

4.10. Maintenance of C. elegans. In this study, two *C. elegans* strains were utilized: (i) transgenic-type (GMC101) dvIs100[unc-54p::A-β-1-42::unc543′UTR + mtl-2p::GFP] and (ii) wild-type (N2), which were provided by the Caenorhabditis Genetics Center (CGC, University of Minnesota). To obtain the synchronous population, frozen-stored *C. elegans* were thawed in the room temperature and transferred to a nematode growth medium (NGM) agar plate seeded with an *E. coli* strain (OD50) and incubated at 20 °C until gravid state, flowed by bleach-synchronization to dissolve worm body and retain eggs. In brief, the gravid adults and eggs were collected with M9 buffer and subjected to centrifugation. A bleach solution consisting of

https://doi.org/10.1021/acschemneuro.3c00293
ACS Chem. Neurosci. 2023, 14, 3143−3155

2.75 mL of Milli-Q water, 1.25 mL of 1 M NaOH, and 1 mL of bleach was added to the worm pellet to release all the adult worms. The resulting mixture was then washed for at least three times with M9 buffer, and the eggs were allowed to hatch overnight in S-complete buffer. The hatched worms were subsequently counted to determine their concentration before further use. Once the worms reached the L4 larval stage, 5-fluoro-2′-deoxyuridine (FudR) was added to inhibit the growth of the offsprings, unless otherwise specified.

4.11. Wild-Type N2 C. elegans Lifespan Assay. *C. elegans* lifespan assay was slightly modified based on a previous study.[53] Briefly, age-synchronized worms in L1-stage ware counted and transferred to a 96-well plate at a concentration of ∼10 worms per well, followed by addition of 30 μL of 0.6 mM FUDR stock solution to each well at L4-stage. Then, 5 μL of test solution, including S-complete buffer-DMSO of positive control, 500 mM NaOH of negative control, and tested target of 5/10/20 μM PG-1, was then added to each well. For each treatment group, a total of 12 wells (*i.e.*, ∼120 worms) were used. The day of drug administration was designated as day 0, and the number of surviving worms was observed and counted under a microscope at 2 day intervals until all the worms were deceased.

4.12. Wild-Type N2 *C. elegans* Brood Size and Hatching Rate Assay. Age-synchronized worms in gravid stage ware randomly assigned to pre-treated (*i.e.*, positive control, negative control, and 5−20 μM PG-1) NGM plate without FUDR at the concentration of 1 worm/well. After 5 h, all the gravid adults were picked out, and the number of hatched eggs was counted for each well. Those eggs were allowed another 1 day to hatch to L1-stage worms. Those eggs that cannot successfully transfer to L1-stage worms would not be counted to contribute to the hatching rate. For each treatment group, a total of 30 wells (*i.e.*, 30 worms) were used.

4.13. Transgenic GMC 101 *C. elegans* Paralysis Assay. Age-synchronized worms in L4-stage were randomly assigned to pre-treated (*i.e.*, positive control, negative control, and 5−20 μM PG-1) NGM plate with FUDR at the concentration of 30 worms/well and further incubated at 25 °C to initiate Aβ. On days 0, 3, 6, and 9, the worms were evaluated and considered paralyzed if they displayed no movement during observation and did not respond to touch-induced stimulation using a platinum wire. Representative worms were subsequently transferred to liquid M9 buffer for additional photographs. To determine the bending frequency, 1 mL of M9 buffer was added to a plate containing the worms, and the number of times of bending in 30 s was counted.

4.14. Staining and Microscopy in Transgenic GMC 101 *C. elegans*. At day 9, a total of 30 worms were randomly selected from different treatment plates and incubated with 1 μM NIAD-4 (0.1% DMSO in M9 buffer) for 4 h at room temperature to result in robust and consistent staining. Subsequently, the worms were transferred onto glass microscopic slides coated with 2% agarose pads containing 40 mM NaN_3 as an anesthetic for imaging. Images were captured using a fluorescence microscope (Olympus IX81) equipped with a ×40 objective and a CY3/DAPI filter. The fluorescence intensity of the images was quantified using ImageJ software and normalized as the corrected total cell fluorescence. Only the head region was considered for analysis due to the presence of high background signal in the guts.

4.15. Transgenic GMC 101 *C. elegans* ROS Assay. 100 worms were randomly selected from day 9 and placed in a tube containing 500 μL of M9 buffer supplemented with 50 μM H2DCF-DA. The tube was then incubated in darkness with intermittent vortexing for a duration of 2 h. Afterward, the worms were washed twice with M9 buffer and transferred to a 96-well plate, with each well containing 20 worms. The fluorescence intensity was measured using a SpectraMax M3 microplate reader (Molecular Devices, CA, USA) under the top-read mode, with an excitation wavelength of 485 nm and an emission wavelength of 530 nm.

■ ASSOCIATED CONTENT

Supporting Information

The Supporting Information is available free of charge at https://pubs.acs.org/doi/10.1021/acschemneuro.3c00293.

AFM images, CD spectra with corresponding secondary structure content, dissociation constant analysis, and antimicrobial analysis (PDF)

■ AUTHOR INFORMATION

Corresponding Author

Jie Zheng − *Department of Chemical, Biomolecular, and Corrosion Engineering, The University of Akron, Akron, Ohio 44325, United States;* orcid.org/0000-0003-1547-3612; Email: zhengj@uakron.edu

Authors

Yijing Tang − *Department of Chemical, Biomolecular, and Corrosion Engineering, The University of Akron, Akron, Ohio 44325, United States*

Dong Zhang − *Department of Chemical, Biomolecular, and Corrosion Engineering, The University of Akron, Akron, Ohio 44325, United States;* orcid.org/0000-0001-7002-7661

Complete contact information is available at: https://pubs.acs.org/10.1021/acschemneuro.3c00293

Author Contributions

Y.T. and J.Z. initiated the idea of this project. Y.T. and D.Z. designed and conducted experiments in vitro. J.Z. supervised this project. The manuscript was written through the inputs of all the authors. All authors have given approval to the final version of the manuscript.

Notes

The authors declare no competing financial interest.

■ ACKNOWLEDGMENTS

We thank the financial support from NSF-CBET-2107619. We also trained three high school students—Bowen Zheng from Copley High School, Alice Xu from Hudson High School, and Keven Gong from Western Reserve Academy—by this project.

■ REFERENCES

(1) Rahman, M. M.; Lendel, C. Extracellular protein components of amyloid plaques and their roles in Alzheimer's disease pathology. *Mol. Neurodegener.* **2021**, *16*, 59.

(2) McManus, R. M. The Role of Immunity in Alzheimer's Disease. *Adv. Biol.* **2022**, *6*, 2101166.

(3) Tang, Y.; Zhang, D.; Gong, X.; Zheng, J. A mechanistic survey of Alzheimer's disease. *Biophys. Chem.* **2022**, *281*, 106735.

(4) LaFerla, F. M.; Oddo, S. Alzheimer's disease: Aβ, tau and synaptic dysfunction. *Trends Mol. Med.* **2005**, *11*, 170−176.

(5) Kent, S. A.; Spires-Jones, T. L.; Durrant, C. S. The physiological roles of tau and Aβ: implications for Alzheimer's disease pathology and therapeutics. *Acta Neuropathol.* **2020**, *140*, 417−447.

(6) Walker, K. A.; Ficek, B. N.; Westbrook, R. Understanding the Role of Systemic Inflammation in Alzheimer's Disease. *ACS Chem. Neurosci.* **2019**, *10*, 3340−3342.

(7) Lin, W. R.; Wozniak, M. A.; Cooper, R. J.; Wilcock, G. K.; Itzhaki, R. F. Herpesviruses in brain and Alzheimer's disease. *J. Pathol.* **2002**, *197*, 395−402.

(8) Tiwari, D.; Singh, V. K.; Baral, B.; Pathak, D. K.; Jayabalan, J.; Kumar, R.; Tapryal, S.; Jha, H. C. Indication of Neurodegenerative Cascade Initiation by Amyloid-like Aggregate-Forming EBV Proteins

and Peptide in Alzheimer's Disease. *ACS Chem. Neurosci.* **2021**, *12*, 3957−3967.
(9) MacDonald, A. B.; Miranda, J. M. Concurrent neocortical borreliosis and Alzheimer's disease. *Hum. Pathol.* **1987**, *18*, 759−761.
(10) Riviere, G. R.; Riviere, K.; Smith, K. Molecular and immunological evidence of oral Treponema in the human brain and their association with Alzheimer's disease. *Oral Microbiol. Immunol.* **2002**, *17*, 113−118.
(11) Alonso, R.; Pisa, D.; Aguado, B.; Carrasco, L. Identification of fungal species in brain tissue from Alzheimer's disease by next-generation sequencing. *J. Alzheim. Dis.* **2017**, *58*, 55−67.
(12) Lövheim, H.; Olsson, J.; Weidung, B.; Johansson, A.; Eriksson, S.; Hallmans, G.; Elgh, F. Interaction between cytomegalovirus and herpes simplex virus type 1 associated with the risk of Alzheimer's disease development. *J. Alzheim. Dis.* **2018**, *61*, 939−945.
(13) Akiyama, H.; Barger, S.; Barnum, S.; Bradt, B.; Bauer, J.; Cole, G. M.; Cooper, N. R.; Eikelenboom, P.; Emmerling, M.; Fiebich, B. L. Inflammation and Alzheimer's disease. *Neurobiol. Aging* **2000**, *21*, 383−421.
(14) Kamer, A. R.; Craig, R. G.; Pirraglia, E.; Dasanayake, A. P.; Norman, R. G.; Boylan, R. J.; Nehorayoff, A.; Glodzik, L.; Brys, M.; de Leon, M. J. TNF-α and antibodies to periodontal bacteria discriminate between Alzheimer's disease patients and normal subjects. *J. Neuroimmunol.* **2009**, *216*, 92−97.
(15) Alonso, R.; Pisa, D.; Rábano, A.; Rodal, I.; Carrasco, L. Cerebrospinal fluid from Alzheimer's disease patients contains fungal proteins and DNA. *J. Alzheim. Dis.* **2015**, *47*, 873−876.
(16) Panza, F.; Lozupone, M.; Solfrizzi, V.; Watling, M.; Imbimbo, B. P. Time to test antibacterial therapy in Alzheimer's disease. *Brain* **2019**, *142*, 2905.
(17) Fulop, T.; Witkowski, J. M.; Bourgade, K.; Khalil, A.; Zerif, E.; Larbi, A.; Hirokawa, K.; Pawelec, G.; Bocti, C.; Lacombe, G.; et al. Can an Infection Hypothesis Explain the Beta Amyloid Hypothesis of Alzheimer's Disease? *Front. Aging Neurosci.* **2018**, *10*, 224.
(18) Shanmugam, N.; Baker, M. O. D. G.; Ball, S. R.; Steain, M.; Pham, C. L. L.; Sunde, M. Microbial functional amyloids serve diverse purposes for structure, adhesion and defence. *Biophys. Rev.* **2019**, *11*, 287−302.
(19) Javed, I.; Zhang, Z.; Adamcik, J.; Andrikopoulos, N.; Li, Y.; Otzen, D. E.; Lin, S.; Mezzenga, R.; Davis, T. P.; Ding, F.; et al. Accelerated amyloid beta pathogenesis by bacterial amyloid FapC. *Adv. Sci.* **2020**, *7*, 2001299.
(20) Tetz, G.; Tetz, V. Bacterial extracellular DNA promotes β-amyloid aggregation. *Microorganisms* **2021**, *9*, 1301.
(21) Kumar, D. K. V.; Choi, S. H.; Washicosky, K. J.; Eimer, W. A.; Tucker, S.; Ghofrani, J.; Lefkowitz, A.; McColl, G.; Goldstein, L. E.; Tanzi, R. E.; et al. Amyloid-β peptide protects against microbial infection in mouse and worm models of Alzheimer's disease. *Sci. Transl. Med.* **2016**, *8*, 340ra72.
(22) Calabrese, A. N.; Liu, Y.; Wang, T.; Musgrave, I. F.; Pukala, T. L.; Tabor, R. F.; Martin, L. L.; Carver, J. A.; Bowie, J. H. The amyloid fibril-forming properties of the amphibian antimicrobial peptide uperin 3.5. *ChemBioChem* **2016**, *17*, 239−246.
(23) Jang, H.; Arce, F. T.; Mustata, M.; Ramachandran, S.; Capone, R.; Nussinov, R.; Lal, R. Antimicrobial protegrin-1 forms amyloid-like fibrils with rapid kinetics suggesting a functional link. *Biophys. J.* **2011**, *100*, 1775−1783.
(24) Zhao, H.; Sood, R.; Jutila, A.; Bose, S.; Fimland, G.; Nissen-Meyer, J.; Kinnunen, P. K. J. Interaction of the antimicrobial peptide pheromone Plantaricin A with model membranes: Implications for a novel mechanism of action. *Biochim. Biophys. Acta Biomembr.* **2006**, *1758*, 1461−1474.
(25) Urrutia, R.; Cruciani, R. A.; Barker, J. L.; Kachar, B. Spontaneous polymerization of the antibiotic peptide magainin 2. *FEBS Lett.* **1989**, *247*, 17−21.
(26) Juhl, D. W.; Glattard, E.; Lointier, M.; Bampilis, P.; Bechinger, B. The Reversible Non-covalent Aggregation Into Fibers of PGLa and Magainin 2 Preserves Their Antimicrobial Activity and Synergism. *Front. Cell. Infect. Microbiol.* **2020**, *10*, 526459.
(27) Caillon, L.; Killian, J. A.; Lequin, O.; Khemtémourian, L. Biophysical investigation of the membrane-disrupting mechanism of the antimicrobial and amyloid-like peptide dermaseptin S9. *PLoS One* **2013**, *8*, No. e75528.
(28) Kagan, B. L.; Jang, H.; Capone, R.; Teran Arce, F.; Ramachandran, S.; Lal, R.; Nussinov, R. Antimicrobial properties of amyloid peptides. *Mol. Pharm.* **2011**, *9*, 708−717.
(29) Wang, L.; Liu, Q.; Chen, J.-C.; Cui, Y.-X.; Zhou, B.; Chen, Y.-X.; Zhao, Y.-F.; Li, Y.-M. Antimicrobial activity of human islet amyloid polypeptides: An insight into amyloid peptides' connection with antimicrobial peptides. *Biol. Chem.* **2012**, *393*, 641−646.
(30) Park, S.-C.; Moon, J. C.; Shin, S. Y.; Son, H.; Jung, Y. J.; Kim, N.-H.; Kim, Y.-M.; Jang, M.-K.; Lee, J. R. Functional characterization of alpha-synuclein protein with antimicrobial activity. *Biochem. Biophys. Res. Commun.* **2016**, *478*, 924−928.
(31) Zheng, H.; Li, H.; Zhang, J.; Fan, H.; Jia, L.; Ma, W.; Ma, S.; Wang, S.; You, H.; Yin, Z.; et al. Serum amyloid A exhibits pH dependent antibacterial action and contributes to host defense against Staphylococcus aureus cutaneous infection. *J. Biol. Chem.* **2020**, *295*, 2570−2581.
(32) Ye, M.; Wang, S.; Ji, X.; Tian, Z.; Dai, L.; Si, C. J. A. C.; Materials, H. Nanofibrillated cellulose-based superhydrophobic coating with antimicrobial performance. *Adv. Compos. Hybrid Mater.* **2023**, *6*, 30.
(33) Soscia, S. J.; Kirby, J. E.; Washicosky, K. J.; Tucker, S. M.; Ingelsson, M.; Hyman, B.; Burton, M. A.; Goldstein, L. E.; Duong, S.; et al. The Alzheimer's disease-associated amyloid beta-protein is an antimicrobial peptide. *PLoS One* **2010**, *5*, No. e9505.
(34) Last, N. B.; Miranker, A. D. Common mechanism unites membrane poration by amyloid and antimicrobial peptides. *Proc. Natl. Acad. Sci. U.S.A.* **2013**, *110*, 6382−6387.
(35) Gosztyla, M. L.; Brothers, H. M.; Robinson, S. R. Alzheimer's Amyloid-β is an Antimicrobial Peptide: A Review of the Evidence. *J. Alzheim. Dis.* **2018**, *62*, 1495−1506.
(36) Soscia, S. J.; Kirby, J. E.; Washicosky, K. J.; Tucker, S. M.; Ingelsson, M.; Hyman, B.; Burton, M. A.; Goldstein, L. E.; Duong, S.; Tanzi, R. E.; et al. The Alzheimer's disease-associated amyloid β-protein is an antimicrobial peptide. *PLoS One* **2010**, *5*, No. e9505.
(37) Iqbal, U. H.; Zeng, E.; Pasinetti, G. M. The use of antimicrobial and antiviral drugs in Alzheimer's disease. *Int. J. Mol. Sci.* **2020**, *21*, 4920.
(38) Bourgade, K.; Garneau, H.; Giroux, G.; Le Page, A. Y.; Bocti, C.; Dupuis, G.; Frost, E. H.; Fülöp, T. β-Amyloid peptides display protective activity against the human Alzheimer's disease-associated herpes simplex virus-1. *Biogerontology* **2015**, *16*, 85−98.
(39) Tang, Y.; Zhang, D.; Gong, X.; Zheng, J. Repurposing of intestinal defensins as multi-target, dual-function amyloid inhibitors via cross-seeding. *Chem. Sci.* **2022**, *13*, 7143−7156.
(40) Zhang, Y.; Liu, Y.; Tang, Y.; Zhang, D.; He, H.; Wu, J.; Zheng, J. Antimicrobial α-defensins as multi-target inhibitors against amyloid formation and microbial infection. *Chem. Sci.* **2021**, *12*, 9124−9136.
(41) Fahrner, R. L.; Dieckmann, T.; Harwig, S. S.; Lehrer, R. I.; Eisenberg, D.; Feigon, J. Solution structure of protegrin-1, a broad-spectrum antimicrobial peptide from porcine leukocytes. *Chem. Biol.* **1996**, *3*, 543−550.
(42) Aumelas, A.; Mangoni, M.; Roumestand, C.; Chiche, L.; Despaux, E.; Grassy, G.; Calas, B.; Chavanieu, A. Synthesis and solution structure of the antimicrobial peptide protegrin-1. *Eur. J. Biochem.* **1996**, *237*, 575−583.
(43) Jang, H.; Ma, B.; Woolf, T. B.; Nussinov, R. Interaction of protegrin-1 with lipid bilayers: membrane thinning effect. *Biophys. J.* **2006**, *91*, 2848−2859.
(44) Wi, S.; Kim, C. Pore structure, thinning effect, and lateral diffusive dynamics of oriented lipid membranes interacting with antimicrobial peptide protegrin-1: 31P and 2H solid-state NMR study. *J. Phys. Chem. B* **2008**, *112*, 11402−11414.
(45) Ma, B.; Nussinov, R. Selective molecular recognition in amyloid growth and transmission and cross-species barriers. *J. Mol. Biol.* **2012**, *421*, 172−184.

https://doi.org/10.1021/acschemneuro.3c00293
ACS Chem. Neurosci. 2023, 14, 3143−3155

(46) Ren, B.; Zhang, Y.; Zhang, M.; Liu, Y.; Zhang, D.; Gong, X.; Feng, Z.; Tang, J.; Chang, Y.; Zheng, J. Fundamentals of cross-seeding of amyloid proteins: an introduction. *J. Mater. Chem. B* **2019**, *7*, 7267−7282.
(47) Tang, Y.; Zhang, D.; Chang, Y.; Zheng, J. Atrial Natriuretic Peptide Associated with Cardiovascular Diseases Inhibits Amyloid-β Aggregation via Cross-Seeding. *ACS Chem. Neurosci.* **2022**, *14*, 312−322.
(48) Hirota-Nakaoka, N.; Hasegawa, K.; Naiki, H.; Goto, Y. Dissolution of β2-microglobulin amyloid fibrils by dimethylsulfoxide. *J. Biochem.* **2003**, *134*, 159−164.
(49) Jing, Y.; Wang, R.; Wang, Q.; Xiang, Z.; Li, Z.; Gu, H.; Wang, X. J. A. C.; Materials, H. An overview of surface-enhanced Raman scattering substrates by pulsed laser deposition technique: fundamentals and applications. *Adv. Compos. Hybrid Mater.* **2021**, *4*, 885−905.
(50) Kalmankar, N. V.; Hari, H.; Sowdhamini, R.; Venkatesan, R. Disulfide-Rich Cyclic Peptides from Clitoria ternatea Protect against β-Amyloid Toxicity and Oxidative Stress in Transgenic Caenorhabditis elegans. *J. Med. Chem.* **2021**, *64*, 7422−7433.
(51) Micsonai, A.; Wien, F.; Kernya, L.; Lee, Y.-H.; Goto, Y.; Réfrégiers, M.; Kardos, J. Accurate secondary structure prediction and fold recognition for circular dichroism spectroscopy. *Proc. Natl. Acad. Sci. U.S.A.* **2015**, *112*, No. E3095.
(52) Tang, Y.; Zhang, D.; Robinson, S.; Zheng, J. Inhibition of Pancreatic Cancer Cells by Different Amyloid Proteins Reveals an Inverse Relationship between Neurodegenerative Diseases and Cancer. *Adv. Biol.* **2023**, *20*, 2300070.
(53) Solis, G. M.; Petrascheck, M. Measuring Caenorhabditis elegans life span in 96 well microtiter plates. *J. Vis. Exp.* **2011**, *49*, No. e2496.

https://doi.org/10.1021/acschemneuro.3c00293
ACS Chem. Neurosci. 2023, 14, 3143−3155